A numerical study on waves induced by wheel-rail contact

Yang, Zhen; Li, Zili

Important note
To cite this publication, please use the final published version (if applicable).
Please check the document version above.

A numerical study on waves induced by wheel-rail contact

Zhen Yang, Zili Li*

Delft University of Technology, Section of Railway Engineering, Stevinweg 1, 2628 CN, Delft, the Netherlands

ABSTRACT

Recent finite element (FE) simulations have revealed the generation and propagation of waves in rail surfaces induced by wheel-rail frictional rolling. These waves have rarely been addressed in the literature. This paper presents an in-depth analysis of these waves, aiming to give new insights into the contact mechanics, a research area in which waves have generally been ignored. The study first categorises the simulated contact-induced waves according to their generation mechanisms as impact-induced, creepage-induced and perturbation-induced waves. The link between the generation of perturbation-induced waves and the stick-slip contact mechanism is then explored. Next, by examining the rail surface nodal motion that forms the wave, the creepage-induced wave is demonstrated to be a Rayleigh wave; this result also shows that the explicit FE method can effectively simulate physical contact-induced waves and provide reliable dynamic contact solutions. Finally, FE modelling is presented to investigate the effects of surface cracks on the waves, which may contribute to wave-based crack detection.

1. Introduction

The contact-induced wave phenomenon [1] has rarely been addressed in the study of wheel-rail rolling. One possible reason is that the waves initiated in dynamic frictional rolling contact and influenced by the entire vibrating structures cannot be reproduced by the broadly used contact theories based on the assumptions of a steady state and a half space, e.g., Hertz contact theory [2] and Kalker's theories [3]. The fundamental difficulty lies is the combination of the strongly non-linear friction law and the dynamics of the solids.

To our knowledge, wheel-rail contact-induced waves were first mentioned in [4], in which wheel-rail frictional rolling contact was solved with an explicit finite element method (FEM). Good agreement was achieved when comparing the obtained explicit finite element (FE) contact solution with Hertz contact theory and Kalker's boundary element contact solution, but a small pressure fluctuation existed in the FE results. This fluctuation was considered to be caused by high-frequency vibration and wave propagation in the wheel and rail continua because the FE contact solutions intrinsically include all the relevant vibration modes of the structures and continua and the associated wave propagations [5].

The explicit FEM has since been increasingly employed for the simulation of wheel-rail dynamic contact involving, for example, impact [6–15], flanging [16–18] and friction-induced instability [19]. The overall picture of the contact-induced wave pattern was observed when the authors of this paper simulated the non-steady-state transition

of wheel-rail contact from a single point to two points [18]. The wave was found to be initiated next to the juncture of the adhesion and slip regions in the contact patch, where the maximum surface shear stress is located. After this study, the waves generated by the impacts at an insulated rail joint [11] and a crossing [13] and the waves caused by wheel-rail lateral creepage [19] were reproduced with explicit FE contact models. The explicit integration algorithm is considered to be computationally attractive and naturally suitable for analysing the contact-induced wave propagation because the total dynamic response time that must be modelled is only a few orders of magnitude longer than the stability critical time step [20] and the contact conditions are updated within a small time interval, which facilitates the analysis of high-frequency wave propagation [21].

The aforementioned studies, however, only presented the wave phenomena observed in explicit FE contact simulations. The generation mechanisms and physical characteristics of the simulated waves have not been examined. This study, in this context, first categorises the waves observed in the previous explicit FE wheel-rail contact simulations according to their generation mechanisms as impact-induced, creepage-induced and perturbation-induced waves. The possible link between the generation of perturbation-induced waves and the stick-slip contact behaviour is then discussed. After that, the study analyses the physical characteristics of the creepage-induced wave observed in [19], confirming that the simulated wave is a Rayleigh wave. Although the Rayleigh wave has been extensively proposed to enable detection of the presence of rail cracking [22,23], its practical application to

---
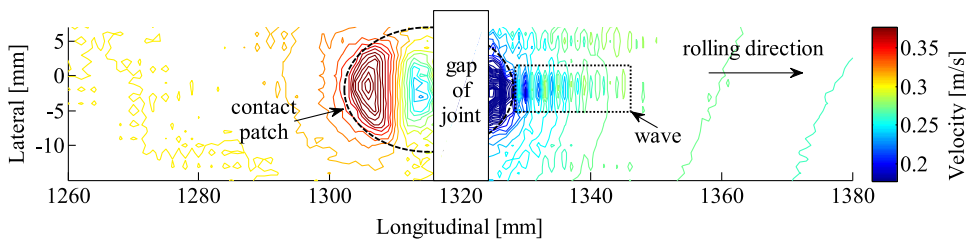
(a) Produced by simulating wheel-IRJ impact [11]
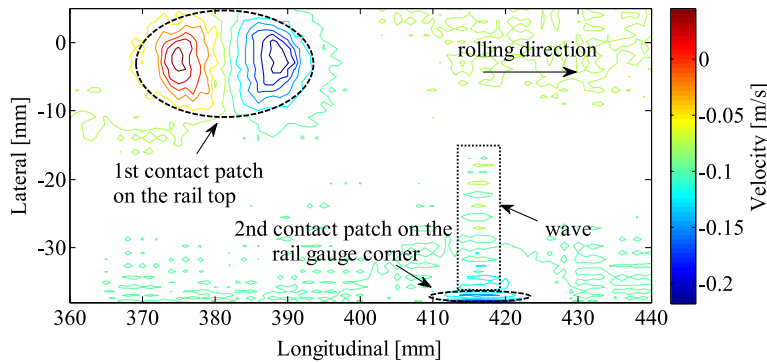
(b) Produced by simulating the wheel-rail two-point contact transition [18]

Fig. 1. Impact-induced wave patterns (see also the animations in [25] and [26]).

field detection is still under development. This study finally presents an explicit FE wheel-rail contact model with a crack to investigate the influence of cracks on the waves, which may contribute to wave-based crack detection.

2. Categorisation and generation mechanisms of the simulated waves

The contact-induced waves discovered in the previous explicit FE wheel-rail contact studies may be categorised according to the generation mechanisms as impact-induced, creepage-induced and perturbation-induced waves. The generation mechanisms of the former two appear to be evident: the significant dynamic effect or kinetic energy [24] induced by the wheel-rail impact or large creepage results in large oscillations of the wheel/rail surface particles in the vicinity of the contact patch. The large local oscillations then propagate and form regular wave patterns. The generation mechanism of the perturbation-induced wave is however less apparent because the perturbation arises during seemingly steady-state rolling.

2.1. Impact-induced waves

The propagation of elastic waves inevitably occurs upon impact [24]. The contour graphs of Fig. 1 present two examples of wheel-rail impact-induced waves. Because the impact excitation is normal to the wheel-rail contact surface, the normal (out-of-plane) nodal vibration velocities play much more important roles than the tangential (in-plane) ones in the formation of the impact-induced wave [11]. The magnitude of the normal nodal velocity on the rail surfaces is indicated by the colour depth of the contour graphs; the leading and trailing edges of the contact patch can thus be identified by the blue and red colours, respectively.

Fig. 1(a) shows an impact-induced wave produced by simulating the impact of a wheel on an insulated rail joint (IRJ); details of the modelling were presented in [11]. When the wheel rolls over the IRJ and hits the rail end on the other side of the joint, an impact-induced wave occurs at the leading edge of the contact patch and propagates forward along the wheel rolling direction. Fig. 1(b) shows another case of an impact-induced wave produced by the wheel-rail two-point contact transition

discussed in [18]. The impact-induced wave arises at the second contact patch on the rail gauge corner immediately after the wheel flange comes into contact with, or hits, the rail gauge corner. The generation and propagation of the impact-induced waves shown in Figs. 1(a) and (b) can be more clearly seen in the animations [25] and [26], respectively.

2.2. Creepage-induced waves

When large wheel-rail creepage occurs, wave patterns embodying the alternation of the compression intensification and relaxation [18] may be generated. Two examples of creepage-induced waves are presented in the contour/vector diagrams in Fig. 2. Fig. 2(a) shows a creepage-induced wave pattern calculated with the explicit FE squeal-exciting contact model presented in [19], in which the wheel-rail rolling contact with a large lateral motion of the wheel is simulated; Fig. 2(b) shows another creepage-induced wave pattern observed in the simulation of the wheel-rail two-point contact transition [18], in which large creepage occurs at the first contact patch on the rail top when the rolling wheel negotiates with the rail via flange contact. The animations corresponding to Fig. 2(a) and (b) displaying the generation and propagation of the creepage-induced wave can be found in [27] and [28], respectively.

In the contour/vector diagrams in Fig. 2, the magnitudes of the normal relative velocities of the wheel/rail nodes are indicated by the colour depth within the contact patches, and the tangential relative velocities between the wheel nodes and the rail nodes, i.e., the micro-slip, are indicated by the blue arrows. The arrows point in the direction of the micro-slip, and their lengths are proportional to the magnitude. Both the normal and tangential nodal velocities contribute to the formation of the creepage-induced wave. The creepage-induced wave appears to propagate parallel to the micro-slip vectors, and the micro-slip in the compression relaxation area (darker colour) is larger than that in the adjacent compression intensification area (lighter colour).

2.3. Perturbation-induced waves

Perturbation-induced waves have also been observed in the previous explicit FE wheel-rail contact simulations: perturbation of the nodal
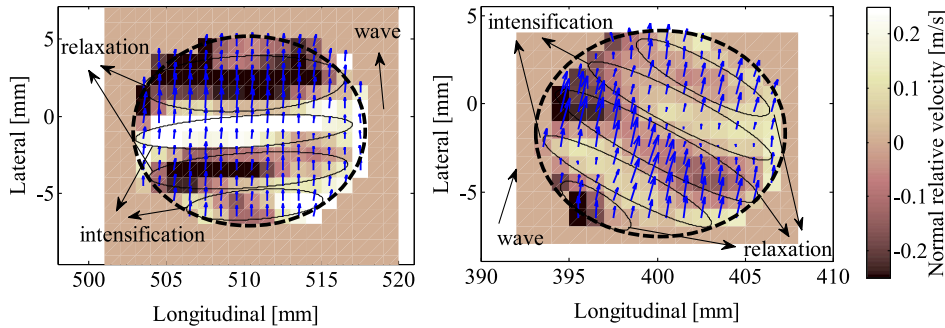
Fig. 2. Creepage-induced wave patterns (see also the animations in [27] and [28]).

(a) Simulated by the squeal-exciting model [19]   (b) Simulated by the contact transition model [18]

velocity suddenly occurs within the contact patch and spreads radially, consequently developing into a wave pattern. The main difference in the perturbation-induced wave compared with the former two wave types is that the perturbation-induced wave, or the perturbation to be precise, may be initiated during seemingly steady-state rolling without the involvement of significant dynamic effects caused by either impacts or large creepage.

Perturbation-induced waves are found to be initiated either close to the leading edge of the contact patch [11] or close to the juncture of the adhesion-slip regions [18]. Two animations of the generation and propagation of perturbation-induced waves are presented in [29] and [30]. The perturbation initiates close to the leading edge of the contact patch in [29] and at the juncture of the adhesion-slip regions in [30]. The animations were obtained by explicit FE simulation of wheel-rail frictional rolling contact without wheel lateral motion (simulation case 1 in [19]).
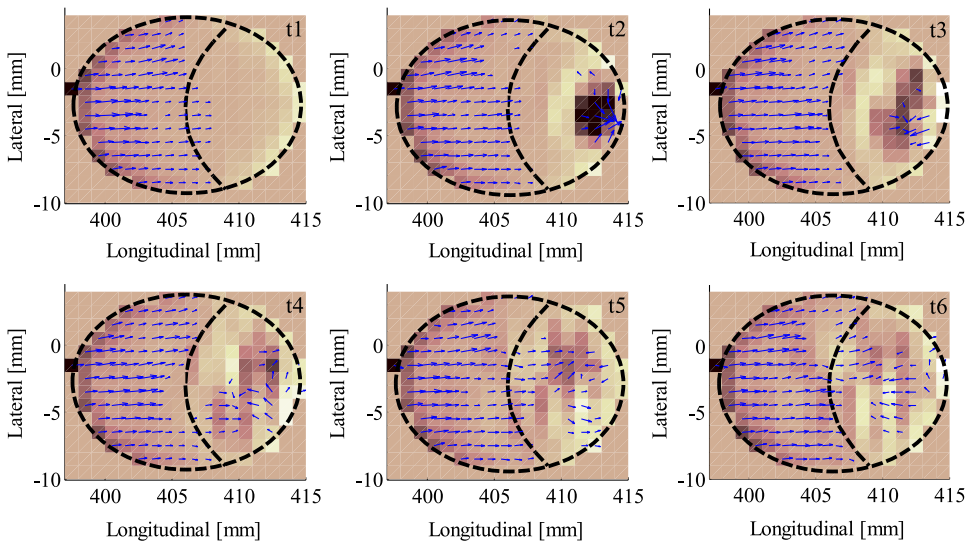
Each animation consists of two windows: the upper window displays the simulated evolution of the wheel-rail relative velocities within the contact patch, and the lower window displays the simulated evolution of the normal and tangential velocities of the rail surface nodes within the entire solution zone (a region on the rail top surface for which the wheel-rail contact solution is output). The wheel-rail relative velocities (in the upper window) can clearly indicate the range of the contact patch and the adhesion-slip regions and thus enable the initiation position of the perturbation to be located, while the rail surface nodal velocities (in the lower window) can more clearly show the wave propagation. Figs. 3(a) and (b), extracted from the upper windows of the animations in [29] and [30], respectively, show the generation processes of the two typical perturbation-induced waves. The range of the contact patch is indicated by the dashed black ovals, and the initial adhesion and slip regions are roughly divided by the dashed curves within the contact patch. The interval between each pair of consecutive graphs in Fig. 3 as well as the time step of the animations in [29] and [30] is 1 μs. Note that the time steps used in all the animations of this paper are more than 10 times larger than the computational time step used in the simulations. In Fig. 3, the perturbation occurs at instant t2 and gradually spreads at instants t3~t6.

The division of the adhesion and slip regions can be determined either by the presence of micro-slip, i.e., micro-slip exists only in the slip region, or by comparing the wheel-rail surface shear stress with the traction bound (the product of the contact pressure and coefficient of friction), i.e., an element is in the slip region if its surface shear stress equals the traction bound, as indicated in Fig. 4. Note that at the initiation locations of the perturbation-induced waves, i.e., close to the leading edge of the contact patch and close to the juncture of the adhesion-slip regions, the surface shear stress is close, but not equal, to the traction bound, as indicated by the two green circles in Fig. 4; therefore, the contact nodes/elements originally in adhesion at these locations are more likely to slip than those elsewhere with an increase of the surface shear stress or a decrease of the traction bound (or a decrease of the pressure when
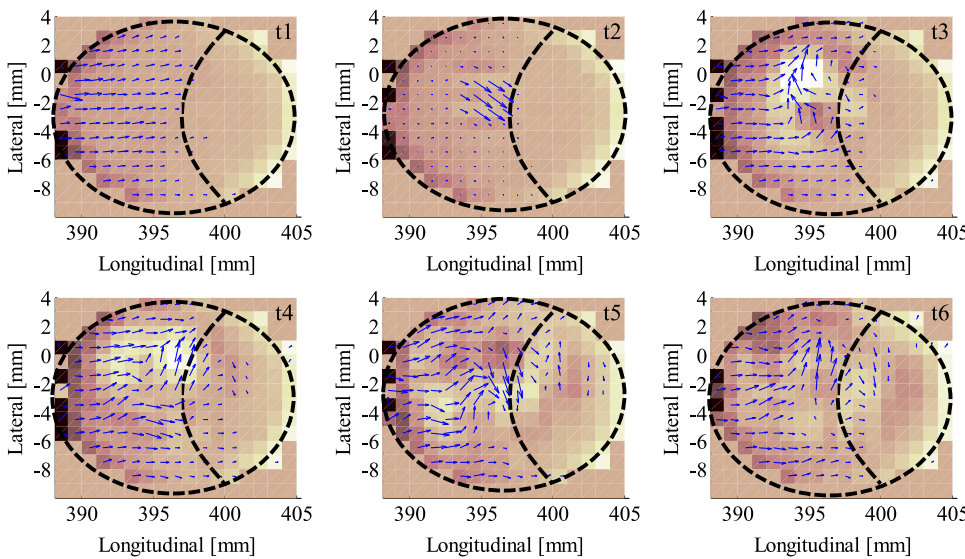
the coefficient of friction is constant). This phenomenon may occur during the dynamic frictional rolling contact in which the contact stresses vary periodically [19]. As shown in Fig. 5 and its corresponding animation in [31], in each period, a moving local peak of the surface shear stress, indicated by the green arrow in Fig. 5, starts at the leading edge of the contact patch, moves towards the trailing edge, and ultimately exits the adhesion region at the juncture of the adhesion-slip region. This local peak or increase of the surface shear stress appears capable of causing sudden slip in the original adhesion area either close to the leading edge of the contact patch or close to the juncture of the adhesion-slip regions, acting as a perturbation within the wheel-rail contact patch and then developing into a wave. Because the variation in the stress distribution is caused by vibration [32], the perturbation-induced waves can be considered to be intrinsically generated by dynamic effects similar to the impact-induced wave and the creepage-induced wave. However, the dynamic effects of the wheel-rail frictional rolling that trigger the perturbation-induced wave may be much less significant than the dynamic effects that initiate the other two types of waves; therefore, the perturbation-induced wave observed in the explicit FE simulations is weaker and lasts for a shorter time.

The initiation location of the perturbation-induced wave can be influenced by the simulated traction condition of the rolling wheel. Figs. 6(a) and (b) extracted from the animations in [33] and [34] show the perturbation-induced waves simulated by a braking wheel rolling model and a tractive wheel rolling model, respectively. The braking rolling is simulated by applying an opposite-direction torque to the wheel axle. The directions of the micro-slip vectors within the slip regions shown in Fig. 6(a) are thus opposite to the wheel rolling direction. Although the time steps used in the animations [33] and [34] (30 μs) are not sufficiently small to capture the entire process of wave generation and propagation, the animations and Fig. 6 still indicate that the perturbation-induced waves generally occur at the leading edge of the contact patch in the simulation of wheel braking, whereas the waves occur more often at the juncture of the adhesion-slip regions in the simulation of wheel traction. The correspondence between the traction/braking condition and the initiation position of the wave might support the actual existence of a perturbation-induced wave during wheel-rail frictional rolling contact because turbulence caused by numerical errors occurs more randomly.

Perturbations occur regularly in the animations in [33] and [34] with a period of approximately 0.6 ms (20 time steps in the animations), corresponding well to the period of the surface shear stress oscillation shown in Fig. 5 and [31]. This result supports the aforementioned finding that the perturbation is generated when the local peak of the surface shear stress periodically passes the boundary of the adhesion region at either the leading edge or the juncture of the adhesion-slip regions. Moreover, Fig. 3 shows that the adhesion region decreases gradually with the spread of the perturbation. The adhesion region can be expected to vanish under certain contact conditions (e.g., by applying a certain coefficient of friction or when the applied traction/braking

Fig. 3. Generation processes of two typical perturbation-induced waves (see also the animations in [29] and [30]).

(a) Perturbation initiates at the leading edge of the contact patch

(b) Perturbation initiates at the juncture of the adhesion-slip regions
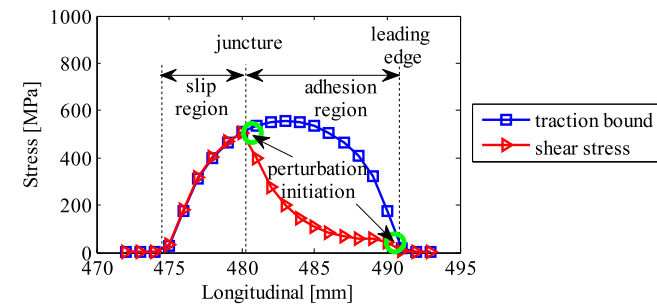

Fig. 4. Contact stress distribution within the contact patch (the green circles indicate the initiation locations of the perturbation: close to the leading edge and the juncture of the adhesion-slip regions).

force exceeds a threshold value), and the stick-slip contact behaviour, characterised by sudden, periodic shear stress drops and markedly influenced by vibration and waves [35], may consequently occur. This study, therefore, seems to link the generation of perturbation-induced

waves with the wheel-rail friction-induced instability – the root cause of squeal [36] and possibly of corrugation [37]. Because the initiation of the perturbation is influenced by the wheel traction/braking condition as analysed above, squeal and corrugation can possibly be mitigated by optimising the traction and braking control strategies based on a better understanding of perturbation-induced waves.

## 3. Physical characteristics of creepage-induced waves

The physical characteristics of the wheel-rail contact-induced wave can be obtained by analysing the nodal motion on the contact surface that forms the wave. As a first attempt to examine the physical characteristics of wheel-rail contact-induced waves, this study limits the analysis of the wave characteristics to creepage-induced waves because more difficulties arise when analysing the surface nodal motion forming impact-induced and perturbation-induced waves: the impact-induced waves shown in Fig. 1 are interfered with either by the reflected wave due to the rail joint (see [38]) or by the waves generated at the contact patch on the rail top (see [28]), and the perturbation-induced wave
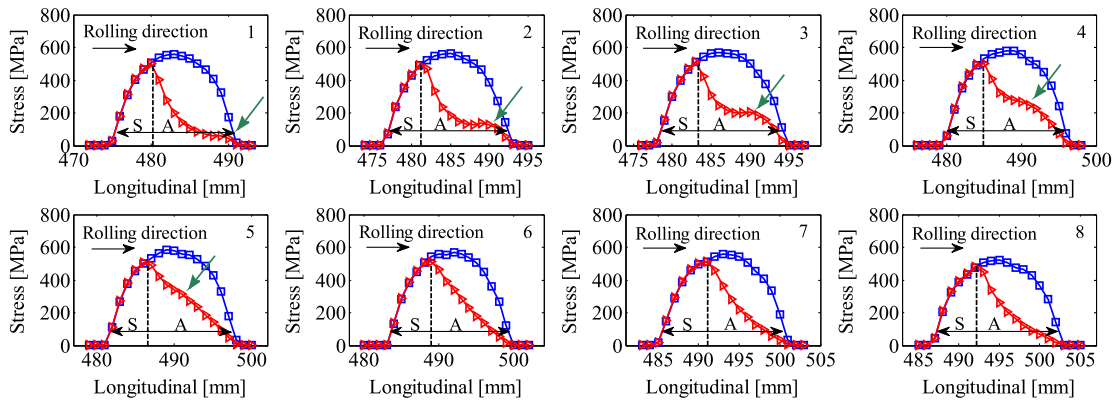
Fig. 5. Periodic surface stress distributions (see also the animation in [31]. blue curve: traction bound; red curve: surface shear stress; A: adhesion region; S: slip region; the green arrows indicate the position of the moving local peak) [19].
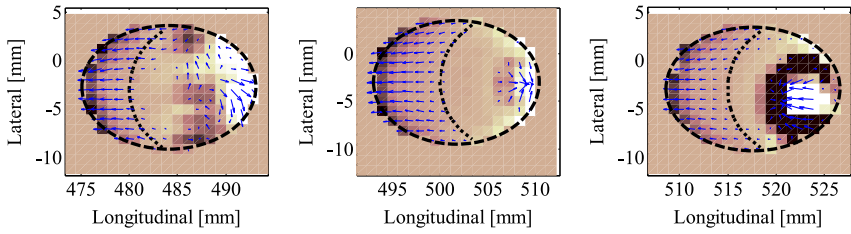
Fig. 6. Perturbation initiations simulated under wheel braking and traction conditions (see also the animations in [33] and [34]).

(a) Wheel braking condition: perturbation is initiated at the leading edge of the contact patch
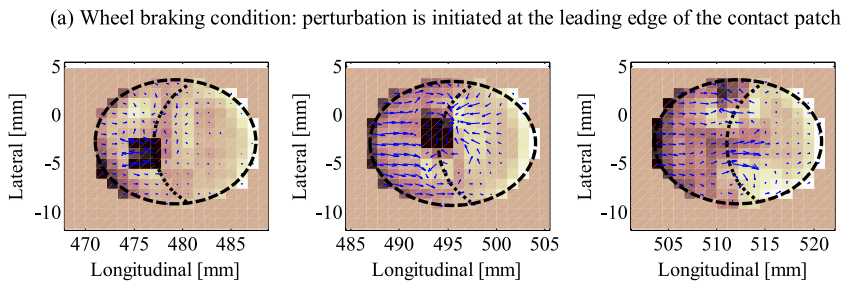
(b) Wheel traction condition: perturbation is initiated at the juncture of the adhesion-slip regions

generated by the much less pronounced dynamic effect is of too short a duration to analyse.

3.1. Preliminary inference of the wave type

A typical creepage-induced wave pattern is presented in the contour/vector diagrams in Fig. 7 (see also [39] for the corresponding animation with a time step of 0.3 μs). The wave is obtained by simulating wheel-rail frictional rolling contact with large lateral motion of the wheel (simulation case 4 in [19]). The wave phenomena can be observed from the distribution of the wheel-rail relative velocities within the contact patch (Fig. 7(a)) and the distribution of the rail surface nodal velocities within the entire solution zone (Fig. 7(b)). The regions of the contact patch are indicated by the dashed black ovals in Fig. 7. In the contour/vector diagrams, the magnitudes and directions of the normal (relative) velocities are indicated by the colour depth, and those of the tangential (relative) velocities are indicated by the red arrows. The creepage-induced wave shown in Fig. 7(a) embodies the alternation of the compression intensification and relaxation within the contact patch (see also Fig. 2), whereas the wave in Fig. 7(b) reflects the vibration velocities of the rail surface nodes. The wavelengths shown in Fig. 7 are approximately 6 mm.

Assuming that the time step used in the animation in [39] – 0.3 μs – is sufficiently small to capture the physical characteristics of the wave, e.g., wave speed and travelling direction, and thus to identify the wave type, three lines of evidence link the simulated creepage-induced

wave to a Rayleigh wave. First, the observed wave is a surface wave formed by the simulated rail surface nodal velocities, as has been shown. Second, both the normal and tangential nodal motions contribute to the formation of the wave, and the direction of the tangential nodal motion is roughly parallel and opposite to the wave propagation direction (see [39]), as will be shown in detail in Section 3.3. Third, the wave speed estimated by dividing the wave travelling distance of 1 mm in each time step by the time step size of 0.3 μs approximates the Rayleigh wave speed in steel (approximately 3 km/s); this result will be further verified in Section 3.3.

3.2. Rayleigh surface wave

A Rayleigh wave is a commonly known type of surface wave formed by retrograde elliptical particle motion on the surface, as shown in Fig. 8: the surface particles move in both the tangential (parallel and opposite to the wave propagation direction) and transverse (normal to the surface) directions, and the phase difference between the tangential motion and the transverse motion is $\pi/2$. The travelling speed of a Rayleigh wave in steel is approximately 3 km/s.

3.3. Nodal motion forming creepage-induced waves

Section 3.1 infers that the simulated creepage-induced wave is a Rayleigh wave based on the assumption that the time step used in the animation in [39] is sufficiently small. To validate this assumption and
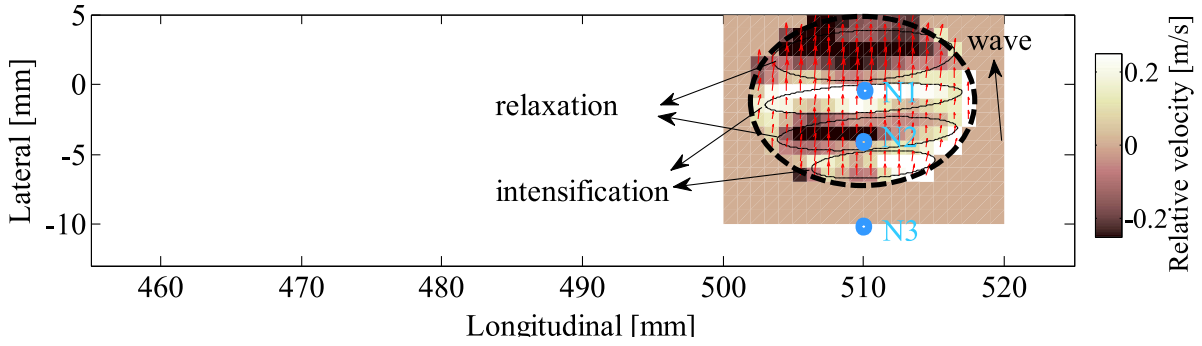
(a) Distribution of the wheel-rail relative velocities within the contact patch
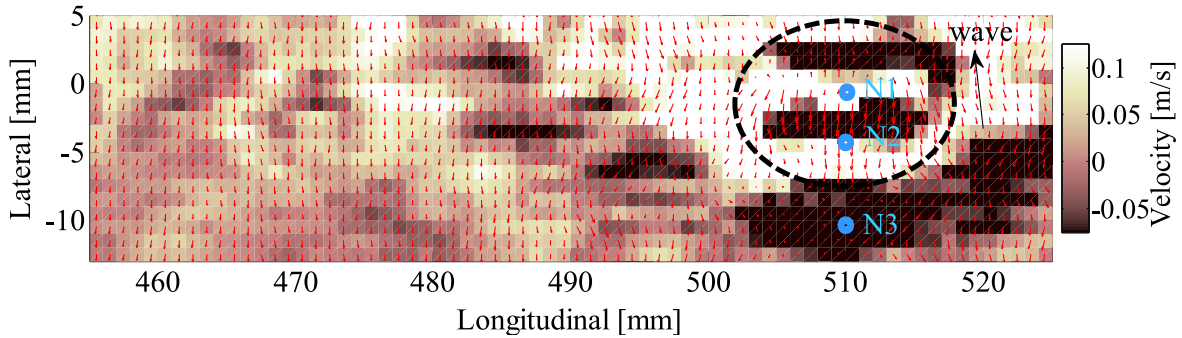
(b) Rail surface nodal velocities within the entire solution zone

Fig. 7. Creepage-induced wave simulated by the wheel lateral motion model (see also the animation in [39]).
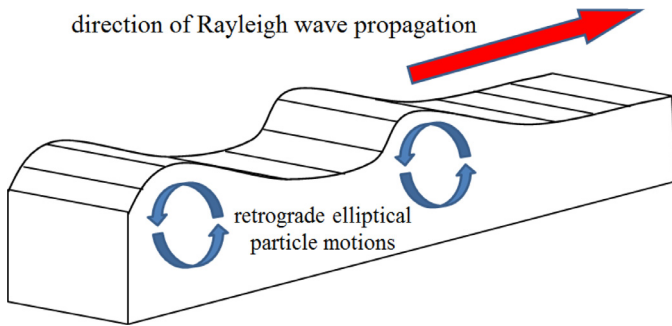

Fig. 8. Retrograde elliptical particle motion of a Rayleigh wave.

the inference made in Section 3.1, this section analyses the simulated nodal motion on the rail surface that forms the creepage-induced wave. The normal and tangential velocities of three rail surface nodes N1~N3, denoted by the solid blue points in Fig. 7, are analysed. The nodes are located approximately on the central lateral line of the contact patch. N1 and N2 are within the contact patch, while N3 is outside the contact patch. The selected nodes have the same longitudinal coordinate of 510 mm and lateral coordinates of 0 mm, −4 mm and −10 mm.

Fig. 9(a) plots the time histories of the simulated normal and tangential velocities of the three selected nodes during the period of 18.18 ms ~18.27 ms (the animation [39] displays the wave in the same period). The tangential nodal velocities have trend components because of the wheel lateral motion prescribed in the simulation. The power spectrum densities of the time histories are correspondingly shown in Fig. 9(b), which indicate that all the nodal velocities are narrow-band signals and have a dominant frequency of approximately 0.495 MHz. The travelling speed of the simulated wave may thus be calculated by multiplying the

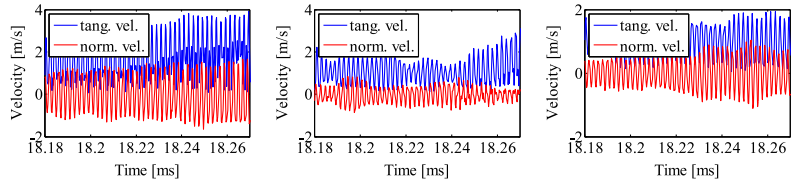wavelength $\lambda_w = 6$ mm and the frequency $f_w = 0.495$ MHz as:

$$v_w = \lambda_w \times f_w \approx 3 \text{ km/s} \tag{1}$$

The good agreement of the wave speed calculated with Eq. (1) and that estimated in Section 3.1 indicates that the time step of the animation [39] is sufficiently small to show the main characteristics of the wave. The bandpass-filtered time histories around the dominant frequency (between 0.48 and 0.51 MHz) are plotted in Fig. 9(c), and close-up views are plotted in Fig. 9(d), which clearly show that both the normal and tangential nodal velocities contribute to the formation of the creepage-induced wave with comparable magnitudes. Fig. 9(e) indicates that the phase differences between the tangential and normal motions of N1 and N2 inside the contact patch are approximately $\pi/2$, corresponding to a Rayleigh wave, whereas that of N3 outside the contact patch is approximately 0.65π, which is possibly caused by the superposition of other waves. Fig. 9(f) shows that the coherence of the tangential and normal motions is 0.98 for N1 and N3 and greater than 0.8 for N2 in the frequency range of interest. Fig. 9(g) plots the retrograde elliptical nodal motion of N1~N3 in displacement, which strongly indicates the presence of a Rayleigh wave (see also [40] for the animations of the corresponding retrograde elliptical nodal motion). The elliptical trails of each node for different cycles do not exactly overlap due to the dynamic effects of wheel-rail frictional rolling.
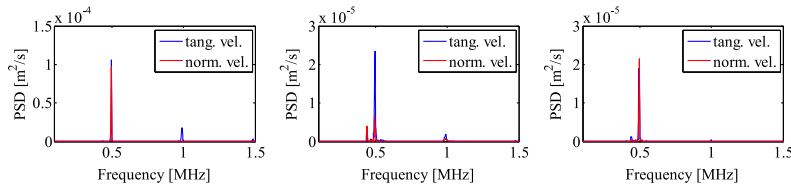
4. Waves generated by a crack

Experimental attempts [22,23] have suggested that Rayleigh waves can be used to detect rail cracks. However, their field application is still under development. As the explicit FEM can effectively capture the contact-induced Rayleigh wave, as analysed in Section 3, this section presents explicit FE modelling of wheel-rail dynamic frictional rolling contact for a rail top surface with a crack to investigate the crack effects on the contact-induced waves. The model was developed from the
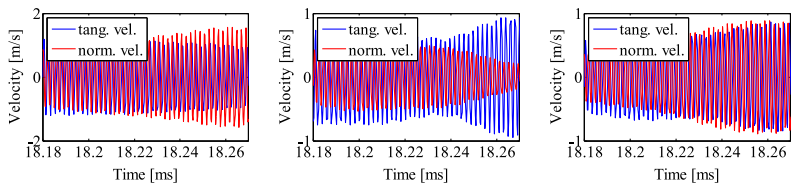
Fig. 9. Simulated surface nodal motion (left, middle and right graphs are for the rail surface nodes N1, N2 and N3, respectively).
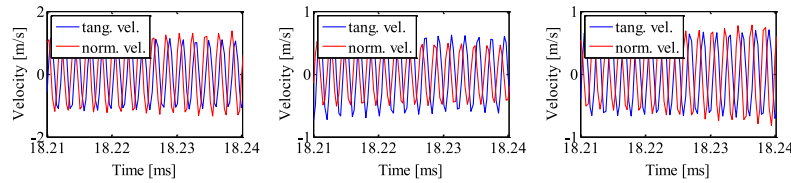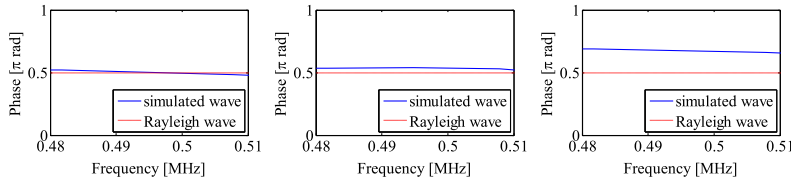
(a) Time histories

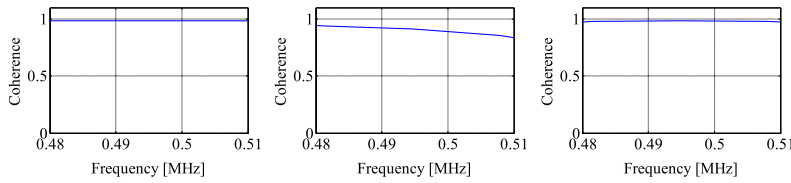(b) Power spectrum densities of the time histories

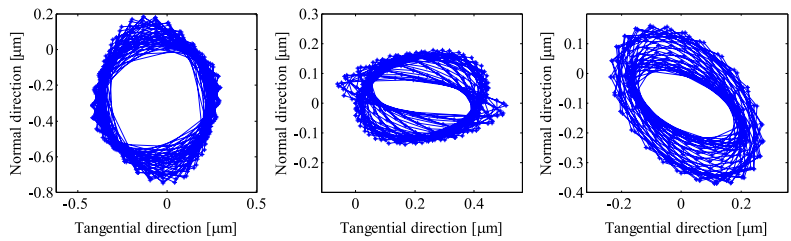(c) Bandpass-filtered time histories

(d) Close-ups of the filtered time histories

(e) Phase difference between the tangential and normal signals

(f) Coherence of the tangential and normal signals

(g) Rayleigh-wave-like elliptical nodal motion (see also the animation in [40])

(a) Addition of a 'seam' to the rail top

(b) The size and position of the modelled crack

Fig. 10. Wheel-rail contact model with a crack on the rail top surface.

(a) Wheel approaches the crack
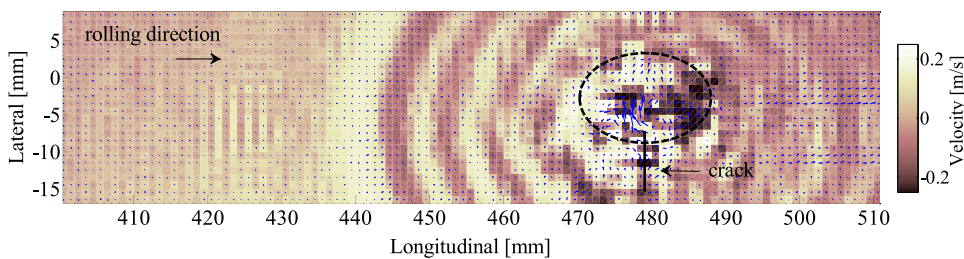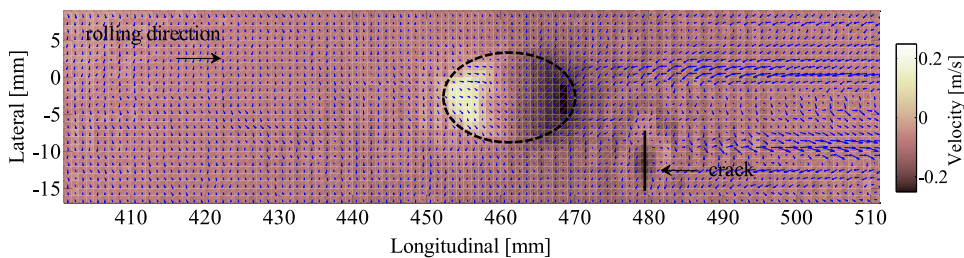
Fig. 11. Contact-induced waves influenced by a crack (see also the animations in [41] and [42]).

(b) Wheel rolls over the crack

wheel-rail contact model without wheel lateral motion (simulation case 1 in [19]) by adding a 'seam' in the rail top, as shown in Fig. 10(a). Fig. 10(b) shows the size and position of the added crack. Contact between the surfaces of the crack is included, with a static coefficient of friction of 0.35.

The contour/vector diagrams in Figs. 11(a) and (b) show the distributions of the rail surface nodal velocities within the entire solution zone when the simulated wheel approaches and rolls over the crack, respectively. The contact patch is indicated by the dashed black oval; the crack is denoted by the bold black line. Wave patterns can be observed in Fig. 11, which are generated at the location of the crack and propagate radially. The wave generated when the wheel rolls over the crack (in Fig. 11(b)) is much stronger than the wave generated when the wheel approaches the crack (in Fig. 11(a)). See [41] and [42] for the corresponding animations with a time step of 1 μs. The characteristics of the waves generated by rail cracks can be investigated in future studies and, together with experimental validation, be used for the development of wave-based detection of rail surface cracks.

5. Conclusions and future research

This paper presented an analysis of the contact-induced waves simulated by explicit FE wheel-rail frictional rolling contact models. According to the generation mechanisms of the waves, this study categorised the simulated waves as impact-induced, creepage-induced and

perturbation-induced waves. All three types of waves should be intrinsically generated by the dynamic effects of the wheel-rail frictional rolling contact; the dynamic effect triggering perturbation-induced waves is however much less significant than those causing impact-induced and creepage-induced waves.

This study also discussed a possible link between the generation of perturbation-induced waves and the stick-slip contact mechanism and found that the initiation location of the perturbation-induced wave can be influenced by the traction/braking condition of the railway wheel: the perturbation generally occurs at the leading edge of the contact patch during wheel braking, whereas it occurs more often at the juncture of the adhesion-slip regions during wheel traction. The cause of periodic perturbation-induced waves should be further studied. A better understanding of perturbation-induced waves may contribute to the mitigation of rail corrugation and squeal as consequences of stick-slip contact by enabling optimisation of the traction and braking control strategies.

This study demonstrated that the simulated creepage-induced wave is a Rayleigh wave by comparing the physical characteristics of the waves. The reproduction of the Rayleigh wave confirmed that the explicit FEM is an effective tool for the analysis of wheel-rail dynamic contact and the associated waves. An explicit FE wheel-rail contact model with a crack in the rail top surface was finally presented to investigate the effects of the crack on the rail surface waves. The generation and propagation of rail surface waves were observed in simulations in which

the wheel approached and rolled over the crack. Further investigation of the physical characteristics of the crack-generated waves and their experimental validation may facilitate the development of a wave-based crack detection method.

References

[1] Hu G, Wriggers P. On the adaptive finite element method of steady-state rolling contact for hyperelasticity in finite deformations. Comput Methods Appl Mech Eng 2002;191:1333–48. https://doi.org/10.1016/s0045-7825(01)00326-7.

[2] Hertz H. Über die berührung fester elastische Körper und über die Harte. J für die reine Angew Math 1882;92:156–71. doi:10.1515/crll.1882.92.156.

[3] Kalker JJ. Three-Dimensional elastic bodies in rolling contact. Netherlands: Springer; 1990 https://doi.org/10.1007/978-94-015-7889-9.

[4] Zhao X, Li ZL. The solution of frictional wheel-rail rolling contact with a 3D transient finite element model: validation and error analysis. Wear 2011;271:444–52. https://doi.org/10.1016/j.wear.2010.10.007.

[5] Zhao X, Li ZL. A three-dimensional finite element solution of frictional wheel-rail rolling contact in elasto-plasticity. Proceed Inst Mech Eng Part J-J Eng Tribol 2015;229:86–100. https://doi.org/10.1177/1350650114543717.

[6] Wen ZF, Jin XS, Zhang WH. Contact-impact stress analysis of rail joint region using the dynamic finite element method. Wear 2005;258:1301–9. https://doi.org/10.1016/j.wear.2004.03.040.

[7] Wiest M, Daves W, Fischer FD, Ossberger H. Deformation and damage of a crossing nose due to wheel passages. Wear 2008;265:1431–8. https://doi.org/10.1016/j.wear.2008.01.033.

[8] Pletz M, Daves W, Ossberger H. A wheel set/crossing model regarding impact, sliding and deformation-explicit finite element approach. Wear 2012;294:446–56. https://doi.org/10.1016/j.wear.2012.07.033.

[9] Zong N, Dhanasekar M. Minimization of railhead edge stresses through shape optimization. Eng Optim 2013;45:1043–60. https://doi.org/10.1080/0305215x.2012.717075.

[10] Molodova M, Li ZL, Nunez A, Dollevoet R. Validation of a finite element model for axle box acceleration at squats in the high frequency range. Comput Struct 2014;141:84–93. https://doi.org/10.1016/j.compstruc.2014.05.005.

[11] Yang Z, Boogaard A, Wei Z, Liu J, Dollevoet R, Li Z. Numerical study of wheel-rail impact contact solutions at an insulated rail joint. Int J Mech Sci 2018;138-139:310–22. https://doi.org/10.1016/j.ijmecsci.2018.02.025.

[12] Yang Z, Boogaard A, Chen R, Dollevoet R, Li Z. Numerical and experimental study of wheel-rail impact vibration and noise generated at an insulated rail joint. Int J Impact Eng 2018;113:29–39. https://doi.org/10.1016/j.ijimpeng.2017.11.008.

[13] Wei Z, Shen C, Li Z, Dollevoet R. Wheel–Rail impact at crossings: relating dynamic frictional contact to degradation. J Comput Nonlinear Dyn 2017;12:041016. https://doi.org/10.1115/1.4035823.

[14] Li Z, Zhao X, Esveld C, Dollevoet R, Molodova M. An investigation into the causes of squats—correlation analysis and numerical modeling. Wear 2008;265:1349–55. https://doi.org/10.1016/j.wear.2008.02.037.

[15] Li ZL, Zhao X, Dollevoet R, Molodova M. Differential wear and plastic deformation as causes of squat at track local stiffness change combined with other track short defects. Veh Syst Dyn 2008;46:237–46. https://doi.org/10.1080/00423110801935855.

[16] Chongyi C, Chengguo W, Ying J. Study on numerical method to predict wheel/rail profile evolution due to wear. Wear 2010;269:167–73. https://doi.org/10.1016/j.wear.2009.12.031.

[17] Vo KD, Zhu HT, Tieu AK, Kosasih PB. FE method to predict damage formation on curved track for various worn status of wheel/rail profiles. Wear 2015;322-323:61–75. https://doi.org/10.1016/j.wear.2014.10.015.

[18] Yang Z, Li ZL, Dollevoet R. Modelling of non-steady-state transition from single-point to two-point rolling contact. Tribol Int 2016;101:152–63. https://doi.org/10.1016/j.triboint.2016.04.023.

[19] Yang Z, Li Z. Numerical modeling of wheel-rail squeal-exciting contact. Int J Mech Sci 2019;153-154:490–9. https://doi.org/10.1016/j.ijmecsci.2019.02.012.

[20] Noh G, Bathe K-J. An explicit time integration scheme for the analysis of wave propagations. Comput Struct 2013;129:178–93. https://doi.org/10.1016/j.compstruc.2013.06.007.

[21] Karttunen AT, von Hertzen R. A numerical study of traveling waves in a viscoelastic cylinder cover under rolling contact. Int J Mech Sci 2013;66:180–91. https://doi.org/10.1016/j.ijmecsci.2012.11.006.

[22] Armitage PR. The use of low-frequency rayleigh waves to detect gauge corner cracking in railway lines. Insight 2002;44:369–72.

[23] Pantano A, Cerniglia D. Simulation of laser generated ultrasound with application to defect detection. Appl Phys A 2008;91:521–8. https://doi.org/10.1007/s00339-008-4442-1.

[24] Reed J. Energy-Losses due to elastic wave-propagation during an elastic impact. J Phys D-Appl Phys 1985;18:2329–37. https://doi.org/10.1088/0022-3727/18/12/004.

[25] Animation for Fig. 1(a), https://youtu.be/fO-P8M1j0oA. [accessed 19.03.15].

[26] Animation for Fig. 1(b), https://youtu.be/ke9yrlX4Jjk. [accessed 19.03.15].

[27] Animation for Fig. 2(a), https://youtu.be/mpTiKS0uZeQ. [accessed 19.03.15].

[28] Animation for Fig. 2(b), https://youtu.be/avYdpZeVzAM. [accessed 19.03.15].

[29] Animation for Fig. 3(a), https://youtu.be/icNEaQ1EMLs. [accessed 19.03.15].

[30] Animation for Fig. 3(b), https://youtu.be/KLaLjIuPG7M. [accessed 19.03.15].

[31] Animation for Fig. 5, https://youtu.be/DaPhrECTLMI. [accessed 19.03.15].

[32] Ouyang H, Nack W, Yuan Y, Chen F. Numerical analysis of automotive disc brake squeal: a review. Int J Veh Noise Vib 2005;1:207. https://doi.org/10.1504/ijvnv.2005.007524.

[33] Animation for Fig. 6(a), https://youtu.be/7Vur6bSQa4c. [accessed 19.03.15].

[34] Animation for Fig. 6(b), https://youtu.be/6-tclZGAjzE. [accessed 19.03.15].

[35] Johnson PA, Savage H, Knuth M, Gomberg J, Marone C. Effects of acoustic waves on stick-slip in granular media and implications for earthquakes. Nature 2008;451:57–60. https://doi.org/10.1038/nature06440.

[36] Thompson DJ. Railway noise and Vibration: mechanisms. Modelling and means of control. Elsevier; 2009.

[37] Sun YQ, Simson S. Wagon–track modelling and parametric study on rail corrugation initiation due to wheel stick-slip process on curved track. Wear 2008;265:1193–201. https://doi.org/10.1016/j.wear.2008.02.043.

[38] Animation of wave reflection, https://youtu.be/tWyWKw9XxRI. [accessed 16.11.22].

[39] Animation for Fig. 7, https://youtu.be/k_E-RF-NdLU. [accessed 19.03.15].

[40] Animation for Fig. 9(g), https://youtu.be/bAPEgB9meQQ. [accessed 19.03.15].

[41] Animation for Fig. 11(a), https://youtu.be/t2A64jm7BrE. [accessed 19.03.15].

[42] Animation for Fig. 11(b), https://youtu.be/9NtVAQMK5eQ. [accessed 19.03.15].